Filtering of Parameterized Nonorographic Gravity Waves in the Met Office Unified Model

CHRISTOPHER D. WARNER

Centre for Atmospheric Science, Department of Applied Mathematics and Theoretical Physics, University of Cambridge, Cambridge, United Kingdom

ADAM A. SCAIFE AND NEAL BUTCHART

Met Office, Exeter, Devon, United Kingdom

(Manuscript received 13 August 2003, in final form 1 November 2004)

ABSTRACT

This paper investigates the vertical filtering of parameterized gravity wave pseudomomentum flux in the troposphere–stratosphere version of the Met Office Unified Model. Gravity wave forcing is parameterized using the Warner and McIntyre spectral gravity wave parameterization. The same amount of isotropic pseudomomentum flux per unit mass is launched from the planetary boundary layer at each grid point. The parameterization models the azimuthally dependent Doppler shifting and breaking of the gravity wave spectrum as it is filtered by the background atmosphere. The result is an anisotropic distribution of pseudomomentum flux among azimuthal sectors that varies greatly with altitude and location. This gives an idealized global climatology of nonorographic gravity waves. The filtering effect of the atmosphere in this climatology is diagnosed using the "zonal anisotropy."

Results show areas where observational measurements could be targeted to find the most prominent features in the gravity wave field. Such areas include, for example, the summer stratosphere where zonal anisotropy is very large and where there is a significant localization in latitude and longitude of patches of high zonal anisotropy. Comparisons are also made with recent observational estimates of gravity wave fluxes and test whether wind filtering of a homogeneous, azimuthally isotropic source is enough to reproduce observed features of the gravity wave field.

1. Introduction

The filtering of gravity waves and the production of gravity-wave-induced forces by changes in the wind and buoyancy frequency with altitude have long been recognized as important effects to include in general circulation models of the atmosphere if a realistic general circulation is to be achieved. Lindzen (1981) parameterized the filtering of monochromatic gravity waves by the background wind, and parameterizations that built on his ideas have been used with great success [e.g., the orographic parameterizations of Palmer et al. (1986) and McFarlane (1987), and the discrete spectral parameterization of Alexander and Dunkerton (1999)]. Holton (1982) applied Lindzen's ideas to discrete spectra consisting of small numbers of monochromatic gravity waves to show that they could provide the "missing" mesospheric forcing and so produce a realistic middle atmosphere circulation in a zonal-averaged mechanistic model.

Fritts and VanZandt (1993) and Fritts and Lu (1993) parameterized the filtering of a continuous spectrum of gravity waves, and several spectral parameterizations have since been produced, for example Hines (1997), Medvedev and Klaassen (1999), Alexander and Dunkerton (1999), and the parameterization used in the current work (Warner and McIntyre 1999, henceforth WM99; see also Warner and McIntyre 2001).

Here we look at the filtering effect of the background atmosphere as it affects the WM99 parameterization. The variation of winds, buoyancy frequency, and density with altitude Doppler shifts the initially azimuthally isotropic model gravity wave spectrum. Wave breaking is modeled as follows: first, waves that have reached a critical layer, that is, waves whose vertical wavenumber m has been Doppler shifted to infinity, are deemed to have broken. Second, waves that exceed an observationally based saturation threshold spectrum are deemed to be breaking. The result is a wind-, buoyancy frequency-, and density-dependent pseudomomentum

Corresponding author address: Chris Warner, Centre for Atmospheric Science, Dept. of Applied Mathematics and Theoretical Physics, University of Cambridge, Wilberforce Road, Cambridge, CB3 0WA, United Kingdom.
E-mail: C.D.Warner@damtp.cam.ac.uk

flux spectrum that depends on the propagation direction of the gravity waves. Using a model rather than observations allows us to impose a source spectrum and so to focus on the effects of filtering.

By modeling the relative amount of filtering of gravity waves propagating in different azimuthal directions, the parameterization is able to compute wave-induced forces that act on the GCM atmosphere. The wave-induced forces affect the background atmosphere, which in turn affect the filtering effect of the background atmosphere. An important, and perhaps the most obvious, effect of this feedback—a quasi-biennial oscillation (QBO)—is present in the GCM simulation and was discussed in two earlier papers (Scaife et al. 2000, 2002) together with other changes to the general circulation that resulted from including parameterized gravity wave forcing in the Unified Model. However, it is useful to look at the filtering effect of the background atmosphere and, in particular, to investigate the extent to which the filtering effect of the troposphere on a model isotropic launched spectrum depends on season and geographical location. Here we also look at the variation with longitude of gravity wave filtering. We find broadly similar behavior to that observed for quasi-stationary waves by Dunkerton and Butchart (1984).

2. Models and diagnostics

a. Met Office Unified Model

The troposphere–stratosphere configuration of the Met Office Unified Model (Cullen 1993) used here is as described in our earlier paper (Scaife et al. 2002). Briefly, the model atmosphere extends from the surface to 0.01 hPa and uses 55 quasi-horizontal vertical levels and a latitude–longitude grid of 2.5° × 3.75°. The configuration uses the physical parameterizations used by Butchart et al. (2000). Orographic gravity waves are parameterized using the Gregory et al. (1998) parameterization and nonorographic waves are parameterized with the WM99 spectral gravity wave parameterization (see section 2b). The two parameterizations run simultaneously but are not coupled together. The penetrative mass flux scheme of Gregory and Rowntree (1990) is used to parameterize convection. The stratospheric water vapor mass mixing ratio used in radiation calculations is fixed at 2.5×10^{-6} above 50 hPa. Annually periodic climatological sea surface temperatures and ozone, used in calculating heating rates, are specified for each month. The well-mixed (same value everywhere) representation is used for other trace gases, including the other greenhouse gases, except for water vapor which is a model variable.

b. Warner and McIntyre parameterization

Full details of the Warner and McIntyre ultrasimple spectral gravity wave parameterization are given in WM99, comparisons with other models are given in Warner and McIntyre (2001), and its impact on the stratosphere in the Met Office Unified Model is described in our earlier paper (Scaife et al. 2002, hereafter SBWS). Here we give a brief description of the scheme. The Warner and McIntyre parameterization models the evolution with altitude of continuous gravity wave spectra launched in each of four azimuthal directions (propagating respectively eastward, northward, westward, and southward).

The launched, or source, spectrum used here is similar to that in WM99 (their Fig. 1) in that it has a low vertical-wavenumber cutoff m_{cut}; here $m_{\text{cut}} = 3.14 \times 10^{-4}$ rad m^{-1}, which corresponds to a vertical wavelength of 20 km. It is linear ($\propto m^1$) between m_{cut} and the characteristic wavenumber m_*; here $m_* = 1.46 \times 10^{-3}$ rad m^{-1}, which corresponds to a vertical wavelength of 4.3 km. It has a -3 power law behavior ($\propto m^{-3}$) above m_*. The launched spectrum differs from that in WM99 in that a constant, latitude-independent, wave stress, or pseudomomentum flux per unit mass $\mathbf{F}_p$ is launched in each of the four azimuthal directions, whereas constant wave energy was launched in WM99. Unfortunately the term pseudomomentum flux is loosely used in the literature to mean both the density-weighted pseudomomentum flux, which we write as $\rho\mathbf{F}_p$, and the pseudomomentum flux per unit mass, which we write as $\mathbf{F}_p$. Equal $\mathbf{F}_p$ in each direction implies that the source spectrum is isotropic relative to the surface. The source spectrum also differs from that in WM99 in that the total (i.e., scalar sum over azimuths) vertical flux of horizontal pseudomomentum $\rho\mathbf{F}_p$ at launch is about 6.6×10^{-3} kg m^{-1} s^{-2}, which is well below saturation at launch (level 3 in the planetary boundary layer of the model which is about 5 km altitude). Note that a launched constant stress or pseudomomentum flux per unit mass $\mathbf{F}_p$ implies a launched density-weighted pseudomomentum flux $\rho\mathbf{F}_p$ that varies with surface pressure, but both $\rho\mathbf{F}_p$ and $\mathbf{F}_p$ are isotropic at launch so that zero net flux is launched. The launched $\rho\mathbf{F}_p$ corresponds to about $\mathbf{F}_p \sim 1.4 \times 10^{-2}$ m^2 s^{-2}. In a hypothetical zero-wind atmosphere, virtually all this flux will survive as it propagates unfiltered to ~100 hPa; $\mathbf{F}_p \sim 1.4 \times 10^{-2}$ m^2 s^{-2} is within the range of current observational estimates for zonally propagating waves in the tropical lower stratosphere (e.g., Sato and Dunkerton 1997; Alexander and Vincent 2000; Ricciardulli and Garcia 2000).

Each azimuthal propagation direction has an associated gravity wave vertical wavenumber spectrum. The evolution of the spectrum with altitude is computed incrementally as a series of discrete changes from one model level to the next. For each altitude increment, changes in the component of background wind in the propagation direction and the buoyancy frequency Doppler shift the spectrum. Then wave breaking is modeled. First, waves that have reached a critical layer; that is, waves whose vertical wavenumber m has been

Doppler shifted to infinity are deemed to have broken. Second, waves that exceed an observationally based empirical m^{-3} saturation spectral ceiling to the Doppler-shifted spectrum are deemed to have broken. This saturation provides stronger breaking than would be obtained from a simpler (and incorrect) assumption of critical level breaking alone. The breaking is stronger because wave amplitudes of waves that have not reached a critical level are only permitted to increase with decreasing density until they reach the saturation spectral ceiling. This leads to a smoother altitude profile of flux deposition than is obtained from critical level breaking alone. Although critical level breaking deposits less flux in total, it deposits it over a smaller altitude range leading locally to large flux deposition near critical levels. The midfrequency approximation to the dispersion relation is used ($\hat{\omega}/k_h = N/m$, where $\hat{\omega}$ is the intrinsic frequency, k_h and m are the horizontal and vertical wavenumbers, respectively, and N is the buoyancy frequency). For each altitude increment the pseudomomentum flux associated with the part of the spectrum above the saturation ceiling is deemed to have been deposited and to have produced a wave-induced horizontal force in the azimuthal propagation direction. The remaining pseudomomentum flux is propagated through the next altitude increment and so on to the top of the model.

As is argued by Lawrence (1997), it may be better to deposit the remaining flux in the top layer or top few layers. Lawrence shows, with a stratosphere–mesosphere mechanistic model together with the Hines parameterization (Hines 1997), that depositing flux at the top of a model that stops at an altitude of about 80 km gives similar results to not depositing in a model that goes up to an altitude of 96 km. However, in our model, depositing remaining flux in the top model layer led to numerical instabilities. Given that the flux here was very small we assumed a transparent lid and allowed flux to escape. In the Tropics, depositing flux affected the upwelling rate and increased the rate at which the shear zones moved downward. Note that allowing the small amount of remaining flux to exit implies that our model does not conserve momentum.

c. Zonal anisotropy diagnostic

The zonal anisotropy α is given by

$$\alpha = \frac{|\mathbf{F}_p(\phi = 0)| - |\mathbf{F}_p(\phi = \pi)|}{|\mathbf{F}_p(\phi = 0)| + |\mathbf{F}_p(\phi = \pi)|}, \quad (1)$$

where $\mathbf{F}_p(\phi)$ is the pseudomomentum flux per unit mass propagating in the azimuthal sector centered on azimuthal direction ϕ. Thus the zonal anisotropy takes values between -1 (no eastward-propagating flux) and 1 (no westward-propagating flux) and takes the value 0 at launch (equal eastward- and westward-propagating fluxes).

3. Observations/model comparison

A comparison of GCM-simulated pseudomomentum fluxes with observational data for Nancy (48°N, 6°E) and Atuona (9°S, 140°W) is given in Figs. 1 and 2, respectively. The figures compare, for the troposphere and stratosphere, the azimuthal distribution of gravity wave energy from radiosonde data with similar model information from the nearest grid point for January, April, July, and October. For the observations the tropospheric data is from the altitude range 1.6 to 11.6 km and the stratospheric data is from the altitude range 11 to 21 km. The corresponding model results are from the 390-hPa and 101-hPa levels. Note that, due to vertical detrending, the radiosonde spectrum is cut at less than 10-km vertical wavelength and degraded at smaller wavelengths, whereas the GCM-simulated source spectrum includes contributions from waves with up to 20-km vertical wavelengths. Although these longer wavelength waves are the least likely to break, some of the differences between observational and GCM figures may arise from their inclusion in the GCM spectrum and not in the radiosonde spectrum. The Nancy data is averaged over the years 1995–2000, the Atuona data is averaged over the years 1995–99, and the model data over 19 years. Also shown are the background zonal and meridional winds from the Met Office data assimilation and the model, again at the nearest grid points to the observations.

Consider first the Nancy data, shown in Fig. 1. Although there are differences between GCM parameterized and observational results, the stratosphere cases show a similar azimuthal distribution in all but the July meridional case. Note that the maximum magnitudes of observational and GCM background wind below are similar and that both the observational and the parameterized troposphere cases are more isotropic than the stratosphere cases. This suggests that observed gravity wave fluxes in the stratosphere may be determined largely by filtering and that the assumption that gravity wave sources are isotropic and near the ground results in reasonable anisotropy in the lower stratosphere. The differences between the tropospheric cases arise because, in reality, wave sources are likely to be azimuthally anisotropic and waves have not propagated far enough for much filtering to take effect. The GCM parameterized results for April, July, and October appear to suffer more filtering by the eastward tropospheric winds than the observational results, that is, the sector centered on 3 o'clock is a smaller fraction of the total for GCM parameterized results than for observational results. This suggests that our model spectrum is more susceptible to filtering than is observed in practice, although other explanations cannot be ruled out. For example, there may be anisotropic sources in the lower stratosphere. We also looked at GCM parameterized results averaged over six years of model run (not shown) to see whether averaging over the same

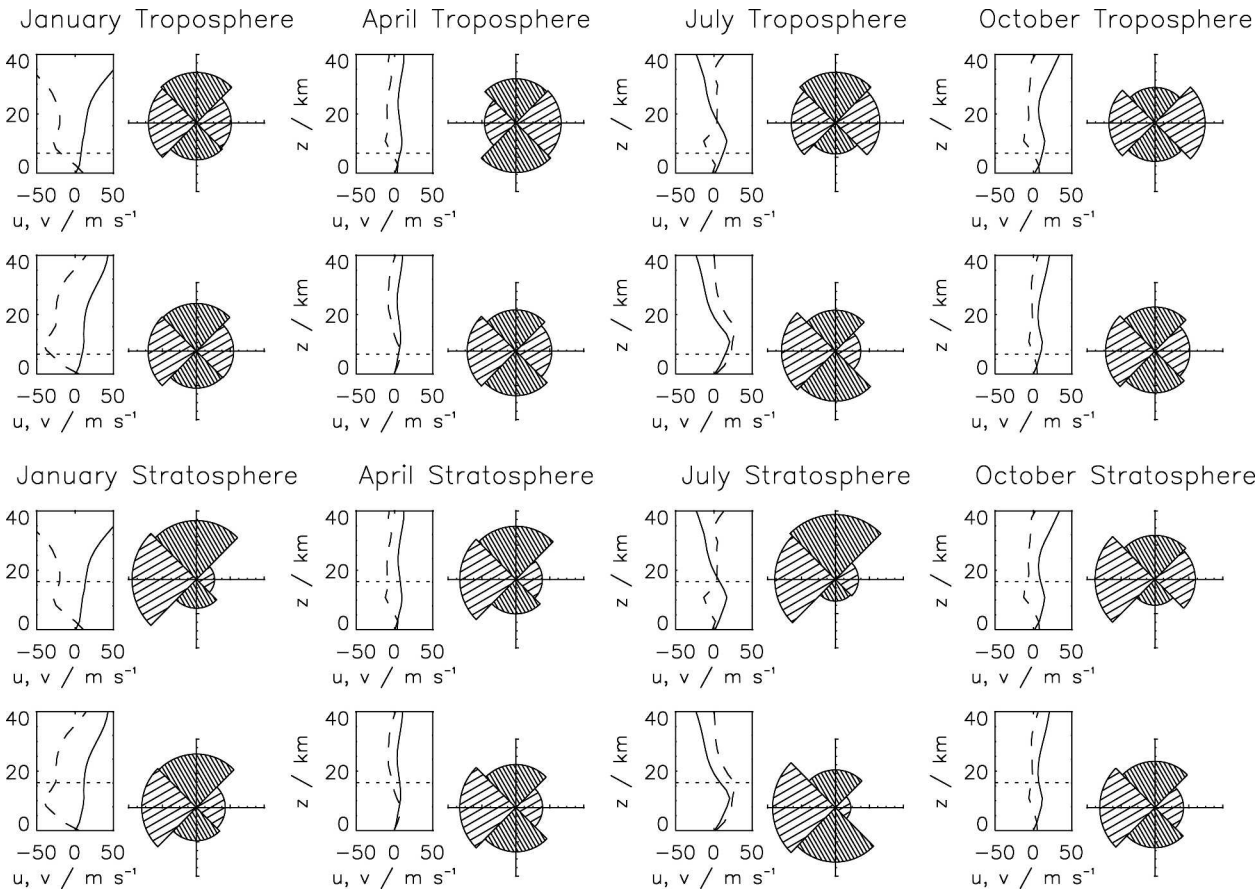

FIG. 1. GCM and observations compared at Nancy for Jan, Apr, Jul, and Oct. For each group of four, the top-left plot shows Met Office Assimilated zonal wind (solid curve) and 10 × meridional wind (dashed curve) for the nearest grid point to Nancy. The top-right plot shows normalized azimuthal distribution of gravity wave energy from radiosonde data. Similarly, the bottom-left plot shows GCM winds for the nearest grid point to Nancy and the bottom-right plot of the group shows the normalized azimuthal distribution of GCM parameterized pseudomomentum flux on the 390-hPa level for the troposphere and on the 101-hPa level for the stratosphere (shown dotted on the wind plot).

number of years as for the observational results made a difference. We found that the 6-yr azimuthal distributions were almost identical to those shown in Fig. 1, especially the zonal sectors.

Figure 2 follows the same pattern as Fig. 1 but shows data for Atuona (9°S, 140°W). It is clear from Fig. 2 that, unlike Fig. 1, the GCM parameterized and observational results are very different and that there are big differences even when the averaged background wind looks broadly similar (e.g., for both the troposphere and stratosphere in January). We looked at GCM parameterized results averaged over five years of model run to see whether averaging over the same number of years as for the observational results made a difference. We also looked at the individual years of model run (not shown). As with Nancy we found that the 5-yr azimuthal distributions were almost identical to those shown in Fig. 2, especially the zonal sectors. The individual model years did show greater variability but could not explain the large differences between observed and GCM data seen in Fig. 2.

These differences may come from the assumption that gravity wave sources are azimuthally isotropic and near the ground. In reality, sources are likely to be neither azimuthally isotropic nor near the ground. One example that illustrates this is the Beres et al. (2002) 2D model study of the effects of tropospheric wind shear on the spectrum of convectively generated gravity waves. They found that the majority of gravity waves are generated in the heating region in the midtroposphere and that there is an increased momentum flux of gravity waves traveling in the opposite direction to the storm-relative wind. Another example of anisotropic gravity wave emission is emission from frontal systems. Charron and Manzini (2002) model emission from fronts with an anisotropic parameterized gravity wave distribution with propagation azimuthal directions in the cross front directions only.

Here we illustrate the effect of launching an azimuthally isotropic gravity wave source spectrum at a range of altitudes in Fig. 3. Figure 3 uses an offline version of the Warner and McIntyre parameterization with as-

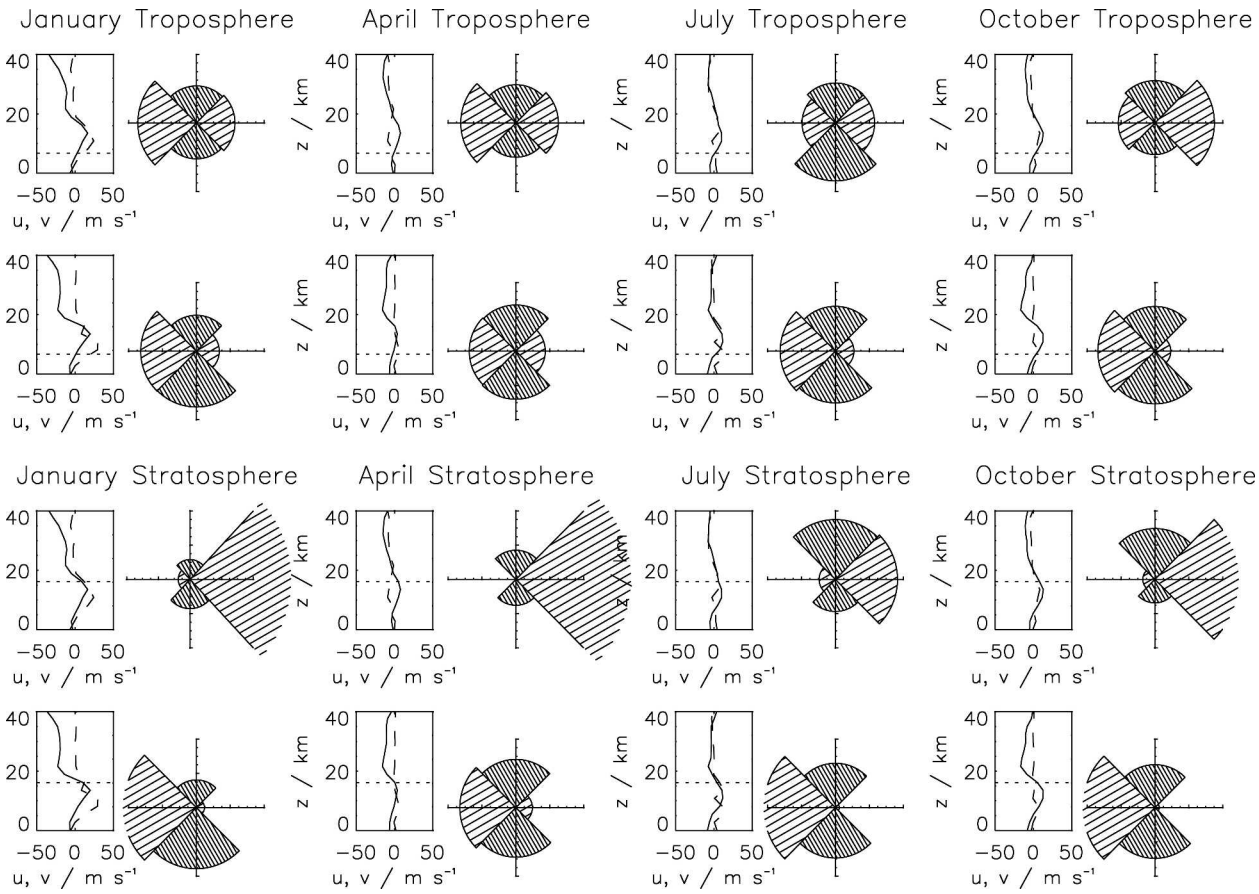

FIG. 2. GCM and observations compared at Atuona: layout as for Fig. 1.

similated wind data for January to show the dependence of anisotropy on launch level. By offline we mean that the parameterization is not part of a GCM and can be used to compute gravity wave fluxes and gravity-wave-induced forces for a user specified vertical profile of wind and buoyancy frequency and user specified launch spectrum parameters. In this instance assimilated wind data is specified and a set of launch altitudes are specified. The fraction of surviving westward-propagating pseudomomentum flux decreases and the fraction of surviving eastward-propagating pseudomomentum flux increases as the launch level is raised. The resulting azimuthal distribution at 101 hPa changes from a distribution similar to the GCM January stratosphere case in Fig. 2 to a distribution that is much closer to the observed January stratosphere case. This is because the waves propagate through a smaller altitude range of eastward shear as the source altitude increases, so a smaller (larger) fraction of the eastward (westward) propagating waves are filtered out. This suggests that, at least for launched isotropically distributed waves, a higher source altitude may be appropriate in the Tropics than at higher latitudes. Thus the approach we have taken in the GCM studies, of launching an isotropic gravity wave source spectrum from a standard altitude has the virtue of simplicity but must be considered to be only a first step toward realism.

As with other parameterizations, the WM99 ultrasimple parameterization makes a number of simplifications to the gravity wave spectral evolution problem to reduce computational cost. Warner and McIntyre (2001) discussed the implications of making these approximations by comparing output from two versions of the ultrasimple spectral parameterization with output from the Warner and McIntyre (1996) full, 3D spectral model. While it would be impractical to attempt to use the full model in a GCM or to look at more than a small number of case studies offline, some straightforward checks have been made. The first such check is to investigate whether time-averaged GCM winds and buoyancy frequencies, when used with an offline version of WM99 parameterization, give similar azimuthal flux distributions to those obtained from averaging individual profiles in the 6-yr GCM run. Figure 4 compares these time-averaged results with observational results at Nancy. The GCM zonal anisotropies in Fig. 4 are similar, but not identical, to those shown in Fig. 1. This is because zonal wind profiles that differ signifi-

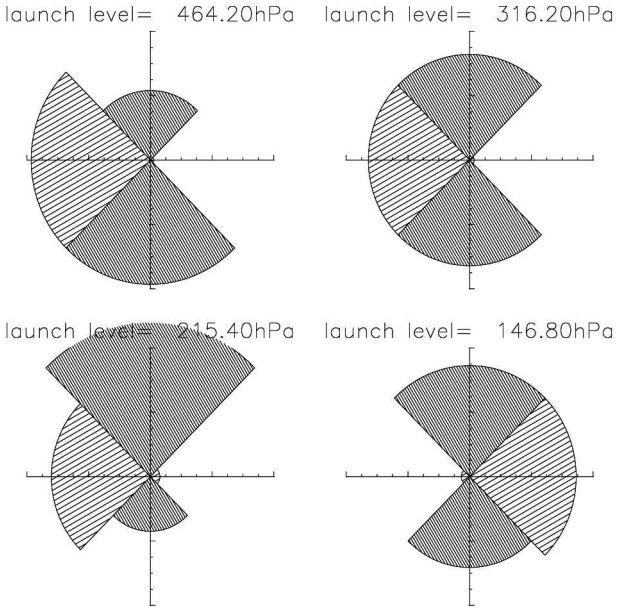

FIG. 3. Azimuthal distribution of pseudomomentum flux at the nearest grid point to Atuona and averaged over the years 1995–99 at an altitude of 101 hPa (about 16 km) for various launch altitudes. Obtained using the offline version of the Warner and McIntyre parameterization with the same Met Office Assimilated wind data as Fig. 2.

cantly from the average profile make a significant contribution to the anisotropy leading to generally greater zonal anisotropies in Fig. 1. The meridional anisotropies show the same effect more clearly. In addition, because the time-averaged meridional wind is small whereas the meridional wind in the individual profiles is often much larger, much less wave breaking happens to meridionally propagating azimuthal sectors in the time-averaged case so the meridional azimuthal sectors make a greater contribution to the total pseudomomentum flux. Figure 5 shows time-averaged results compared with observational results at Atuona. The time-averaged results are affected by averaging in the same way as for Nancy; that is, zonal and meridional anisotropies are generally smaller and meridional azimuthal sectors make a larger contribution to the total flux: compare Figs. 5 and 2.

The second check is to investigate the importance of the back-reflected contribution to the parameterized fluxes. To address this issue requires a spectral model that does not take the hydrostatic, nonrotating approximation to the dispersion relation, such as the Warner and McIntyre (1996) full, 3D spectral model. When the full model is used with the time-averaged background atmosphere data at Nancy and Atuona, the amount of launched pseudomomentum flux that is reflected is never more than 10%. That 10% consists almost entirely of contributions from waves with horizontal wavelengths less than 50 km. Not surprisingly, when azimuthal anisotropy plots such as those in Figs. 1 and 2 (not shown) are compared for the ultrasimple parameterization case and for the full model case including reflection, there are visible differences. However, the differences between azimuthal anisotropy plots for the full model with reflection and the full model without reflection are much smaller. The largest difference is for the July stratosphere case at Nancy where 10% of the eastward propagating flux is reflected. Thus, although the back-reflected flux is important, the wave-breaking flux (deposited by waves that have reached a critical layer or have exceeded the saturation threshold spectrum) dominates.

The third check is to investigate the relative importance of filtering due to waves encountering critical levels and filtering due to waves exceeding the saturation threshold. It is difficult to turn off the saturation threshold in the WM99 parameterization, but it is straightforward to do so in the full, 3D spectral model. For this reason time-averaged background atmosphere data at Nancy have been used to investigate the relative importance of critical layer and saturation filtering in the full model. Because the launched spectrum is not saturated, in the troposphere, where it remains largely below the saturation threshold, critical levels account for most of the filtering. Higher up, in the stratosphere, where more and more of the spectrum exceeds the saturation threshold, critical levels are of secondary importance to saturation threshold filtering in determining the shape of the wave spectrum.

The above three checks indicate that anisotropy data obtained from the WM99 parameterization, rather than from the full, 3D spectral model, should be a good enough approximation for our purposes here.

4. Zonal mean fluxes

Figure 6 shows zonal anisotropy and zonal wind contour lines superimposed. The data shown is an average of 19 years of model run for all of the time steps in each month: January, April, July, and October. Note that the model run includes a QBO. Gravity wave spectral filtering by the zonal wind is clearly illustrated in the January and July plots. In both these plots big changes in zonal anisotropy occur as gravity wave spectra propagate through the tropospheric subtropical jets, leading to the shadows of large negative zonal anisotropy above the jet core. These are seen most clearly above the summer subtropical jets, but are also apparent above the winter subtropical jets. In the shadow region in January, the gross (scalar sum of westward and eastward) flux is 1.91×10^{-3} kg m^{-1} s^{-2}, the net (vector sum of westward and eastward) flux is -1.39×10^{-3} kg m^{-1} s^{-2}, resulting in a zonal anisotropy of -0.73. Similarly, above the summer jet in July, the gross (scalar sum of westward and eastward) flux is 2.2×10^{-3} kg m^{-1} s^{-2}, the net (vector sum of westward and eastward) flux is 1.2×10^{-4} kg m^{-1} s^{-2}, resulting in a

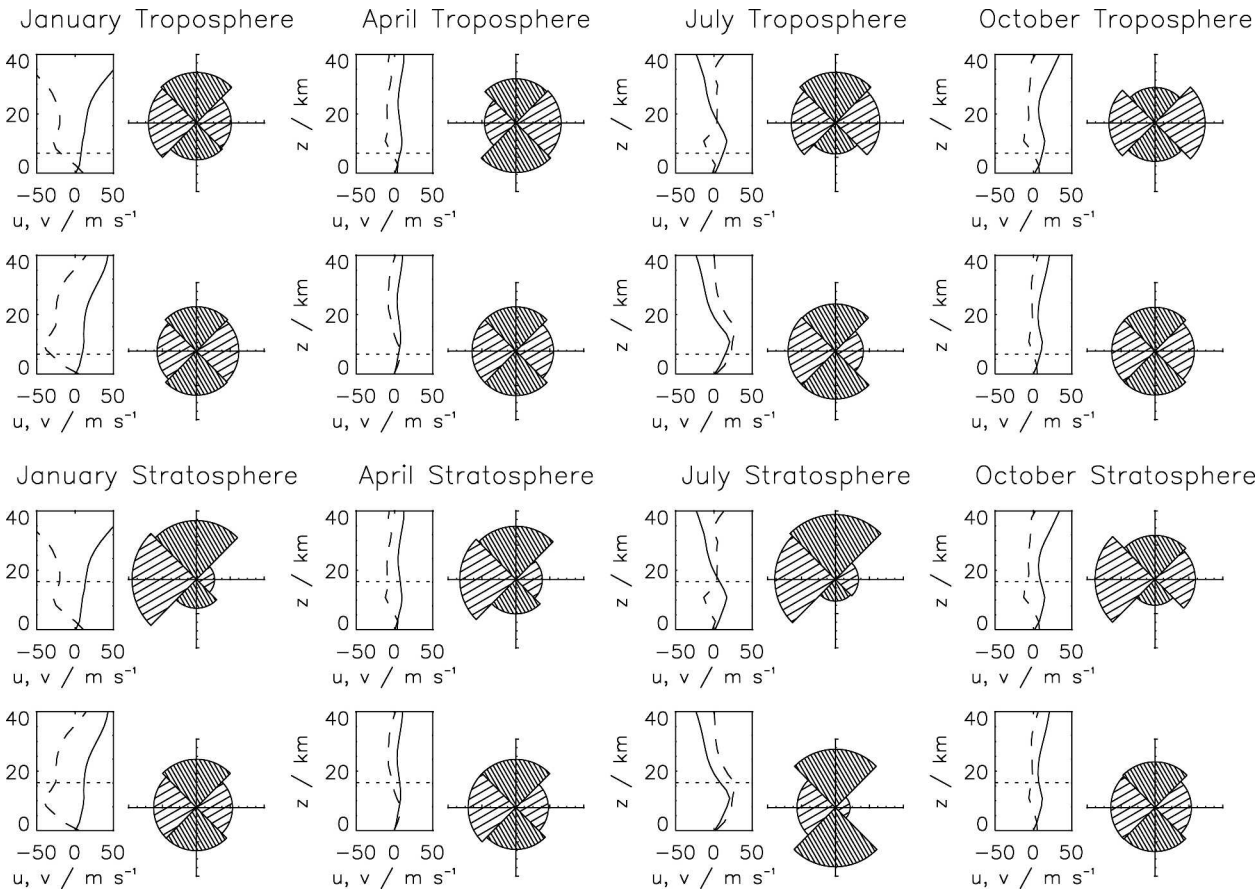

FIG. 4. Time-averaged GCM winds and buoyancy frequencies with offline version of Warner and McIntyre (1999) parameterization and observations compared at Nancy: layout as for Fig. 1.

zonal anisotropy of −0.50. These examples illustrate that the net and gross fluxes can differ by almost an order of magnitude as pointed out by Sato and Dunkerton (1997), albeit for tropical gravity wave observations.

Gravity wave spectral filtering by the stratospheric jets also leads to big changes in zonal anisotropy. The summer hemisphere westward jets preferentially filter out the westward-propagating part of the gravity wave spectrum leading to the shadows of large positive zonal anisotropy and net eastward flux within and above the jet. For example, in summer in the upper stratosphere, the zonal anisotropy exceeds 0.5. The strong eastward winds of the southern winter jet lead to large negative zonal anisotropies throughout most of the stratosphere. The filtering effect of the weaker eastward winds of the northern winter stratospheric jet is less pronounced but is still strong enough to preferentially filter out the eastward-propagating part of the spectrum leading to negative zonal anisotropy within and above the jet (of <-0.5). The effect of these changes in anisotropy and the corresponding deposition of pseudomomentum flux is (SBWS, their section 3a) to roughly halve the strength of the winter westerly jets and reduce the strength of the summer easterly jets.

The shadowing effect of the jets can also be seen in the April and October cases, but anisotropy values are generally lower because the zonal winds are weaker and so filtering of waves is less severe. Figure 7 shows the corresponding net zonal pseudomomentum fluxes. Areas of negative net zonal mean pseudomomentum flux correspond to areas of negative zonal anisotropy (Fig. 6) and areas of positive flux to areas of positive zonal anisotropy. Comparing the two figures, on the one hand, regions of similar zonal anisotropy can have zonal pseudomomentum fluxes that differ greatly (by several orders of magnitude) and, on the other hand, regions of similar zonal pseudomomentum flux can have zonal anisotropies that differ greatly.

Net fluxes and anisotropies show marked differences from year to year in the tropical latitudes. These differences arise from varying phase differences between the annual cycle and the QBO that lead to very different wind patterns and filtering patterns, particularly in April and October. The multiyear averages largely filter out QBO-related effects leaving the persistent an-

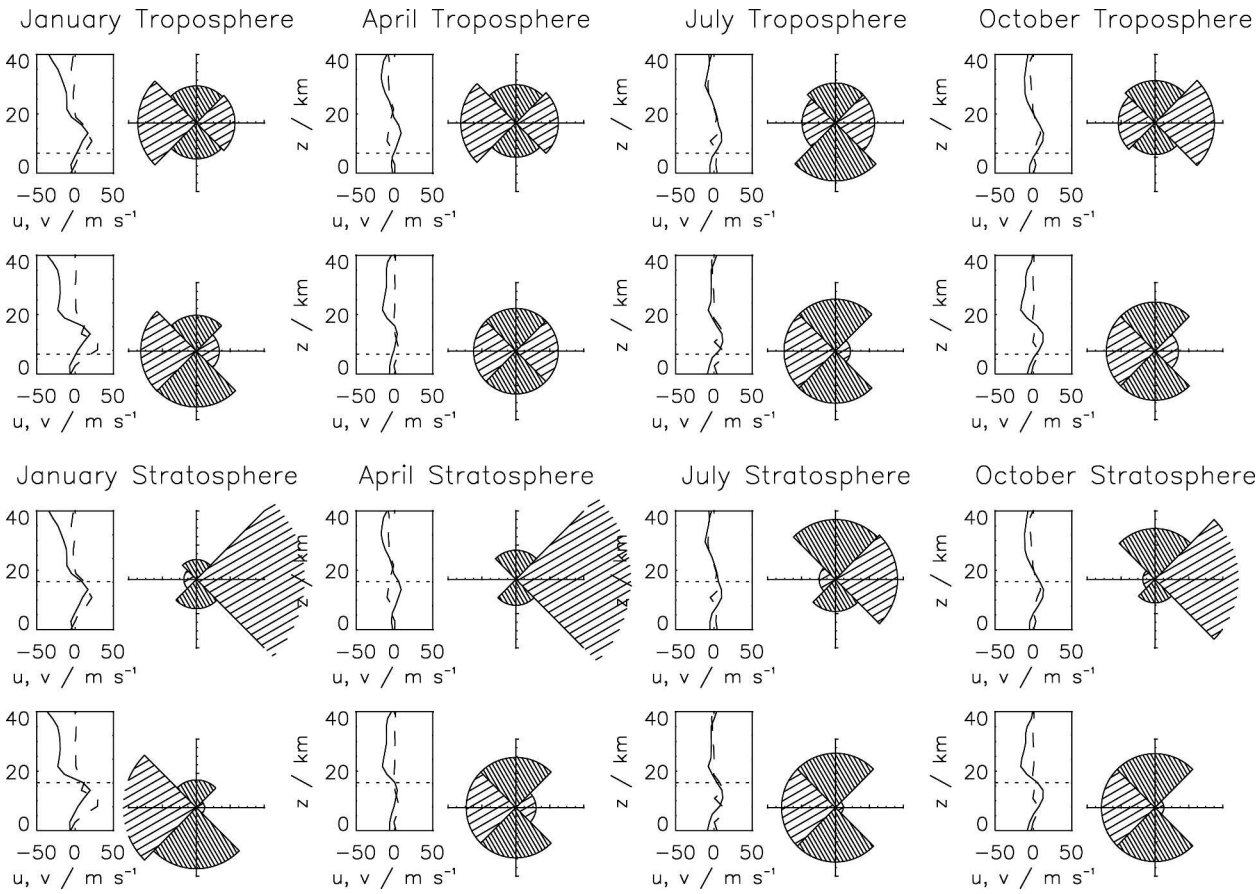

FIG. 5. Time-averaged GCM winds and buoyancy frequencies with offline version of Warner and McIntyre (1999) parameterization and observations compared at Atuona: layout as for Fig. 2.

nual patterns. We will return to the QBO-related effects in section 6.

Now consider the wave-induced acceleration that results from the changes with altitude in pseudomomentum flux and hence in anisotropy (Fig. 8). The regions of large negative wave-induced acceleration in the lower mesosphere in winter are regions of negative anisotropy (Fig. 6) and negative net pseudomomentum flux that are decreasing in magnitude with altitude (Fig. 7).

There are low and high latitude regions of large positive wave-induced acceleration in the lower mesosphere in summer and these are both regions of positive anisotropy (see Fig. 6). For the low latitude cases, the parameterized gravity wave spectrum essentially only consists of eastward-propagating waves (anisotropy >0.9), whereas for the high latitude cases, the gravity wave spectrum varies from nearly isotropic (anisotropy ≈ 0.2) near 80°N in January and near 80°S in July to consisting essentially only of eastward-propagating waves (anisotropy ≈ 0.8) near 60°N in January and 60°S in July. The regions of large positive wave-induced acceleration are regions of positive net pseudomomentum flux that is decreasing in magnitude with altitude (see Fig. 7).

It is clear from Figs. 6 and 7 that there are other latitude and altitude ranges where anisotropy is large and net pseudomomentum flux decreases in magnitude with altitude but where the net wave-induced forces, shown in Fig. 8 (Fig. 3 of SBWS), are small. Two examples, where there is little evidence of large wave-induced forces in Fig. 8, are the region 30°–50°S, 100–10 hPa in January and the region 20°–40°S, 100–10 hPa in July. The reason for this is that the magnitude of the wave-induced acceleration depends very strongly on the background density in the regions where pseudomomentum flux is being deposited.

Thus the filtering of gravity wave pseudomomentum flux by the background atmosphere is consistent with the wave-induced acceleration. However, it is not straightforward to relate the acceleration to any one of anisotropy, net pseudomomentum flux, or net pseudomomentum flux per unit mass because wave breaking at a given altitude and in the atmosphere below affects all three parameters in different ways. Waves approaching critical lines can increase or decrease existing

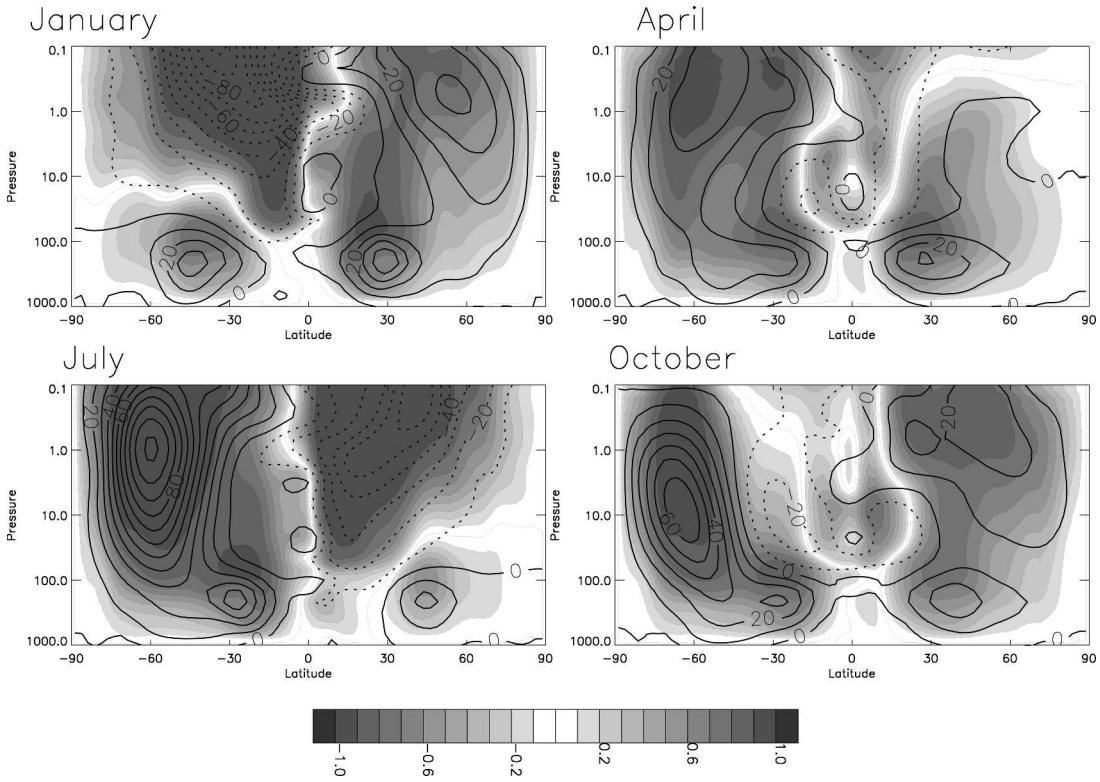

FIG. 6. Zonal mean zonal anisotropy with zonal mean zonal wind contours superimposed. The anisotropy is shown as gray shading with negative contours dashed; contour spacing is 0.1. Positive anisotropy means more eastward-propagating than westward-propagating pseudomomentum flux. The zonal wind is shown as bold contours with negative contours dashed; contour spacing is 10 m s^{-1}. Pressure units for the vertical axis are hPa.

anisotropy depending on the variation with altitude of the background atmosphere below, whereas saturation threshold filtering in constant background wind will always reduce anisotropy. Thus the conditions that favor large wave-induced forces are as follows.

1) An atmosphere well below that has preferentially filtered out waves propagating in one direction over another leading to a large net pseudomomentum flux.
2) Sufficiently high altitude for a low background density and thus a large net pseudomomentum flux per unit mass.
3) Background wind shear that is filtering out waves that are propagating in the direction of the net pseudomomentum flux.

5. Zonal variation of gravity wave filtering

Model anisotropy data

Figure 9 shows zonal anisotropy as a function of latitude and longitude at 101 hPa. Superimposed are contours of maximum eastward wind between this level and the launch altitude, which is a measure of the filtering effect of the wind on the eastward-propagating waves. The shadows that were a prominent feature of the zonal average picture of Fig. 6 are still apparent, particularly in the band of latitudes between 20° and 50°S in January and between 40° and 60°N in July. Over both of these latitude ranges, values of zonal anisotropy are large and negative because of strong eastward winds in the troposphere below. The wider area of strong negative zonal anisotropy at midlatitudes in both winter hemisphere cases is partly the result of tropospheric filtering and partly the result of further filtering in eastward winds below the stratospheric jets. Superimposed on the gross zonal effect of filtering by the tropospheric jets is significant longitudinal variation of filtering, especially in the midlatitude jet streams. However, the areas of large negative zonal anisotropy in the midlatitudes coincide with the areas with largest maximum eastward wind below (cf. the contours of maximum eastward wind between the launch altitude and 101 hPa with the areas of largest negative zonal anisotropy).

The filtering effect of the wind on the westward propagating waves is shown in Fig. 10. The patches of large positive values of zonal anisotropy can be explained by the underlying westward wind values. In other words, changes in modeled anisotropy in the

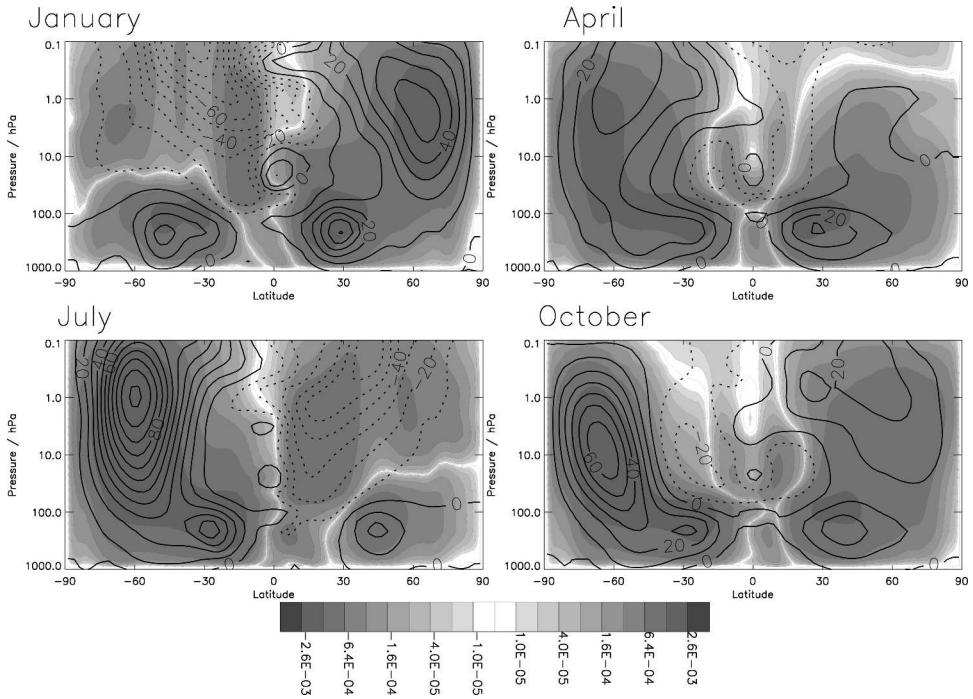

FIG. 7. Zonal mean zonal gravity wave pseudomomentum flux with zonal mean zonal wind contours superimposed. The pseudomomentum flux is shown as gray shading with negative contours dashed; contours are (0, $\pm 1.00 \times 10^{-5}$, $\pm 2.00 \times 10^{-5}$, $\pm 4.00 \times 10^{-5}$, $\pm 8.00 \times 10^{-5}$, $\pm 1.60 \times 10^{-4}$, $\pm 3.20 \times 10^{-4}$, $\pm 6.40 \times 10^{-4}$, $\pm 1.28 \times 10^{-3}$, $\pm 2.56 \times 10^{-3}$, $\pm 5.12 \times 10^{-3}$); units are Pa. The zonal wind is shown as bold contours with negative contours dashed; contour spacing is 10 m s^{-1}. Pressure units for the vertical axis are hPa.

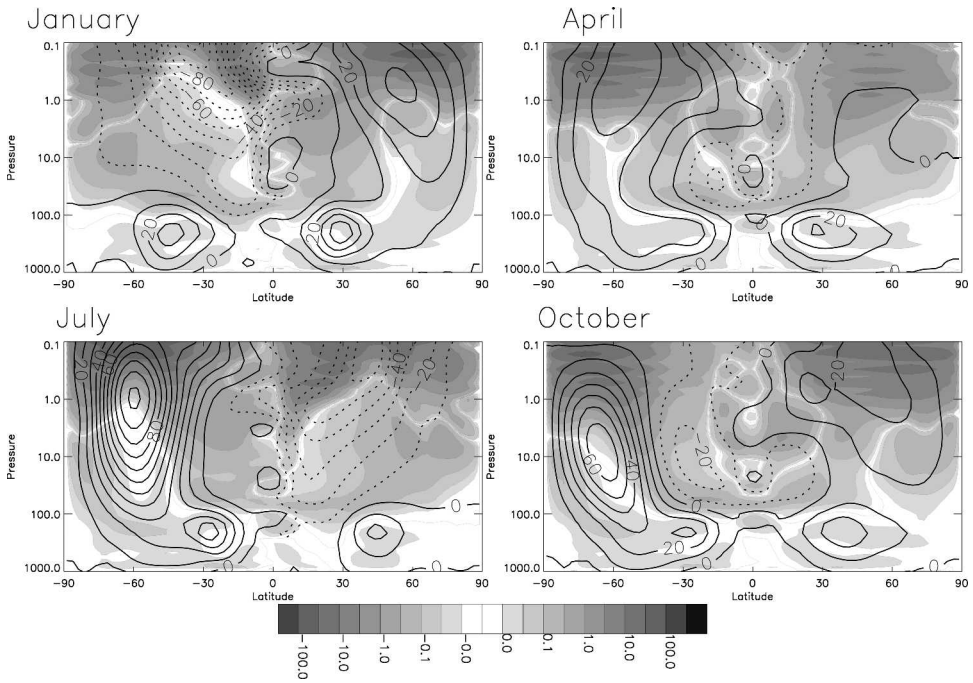

FIG. 8. Zonal mean zonal gravity-wave-induced force per unit mass with zonal mean zonal wind contours superimposed. The wave-induced force per unit mass is shown as gray shading with negative contours dashed; contours are (0.0, ±0.01, ±0.0316, ±0.1, ±0.316, ±1.0, ±3.16, ±10.0, ±31.6, ±100.0), units are m s^{-1} day^{-1}. The zonal wind is shown as bold contours with negative contours dashed; contour spacing is 10 m s^{-1}. Pressure units for the vertical axis are hPa.

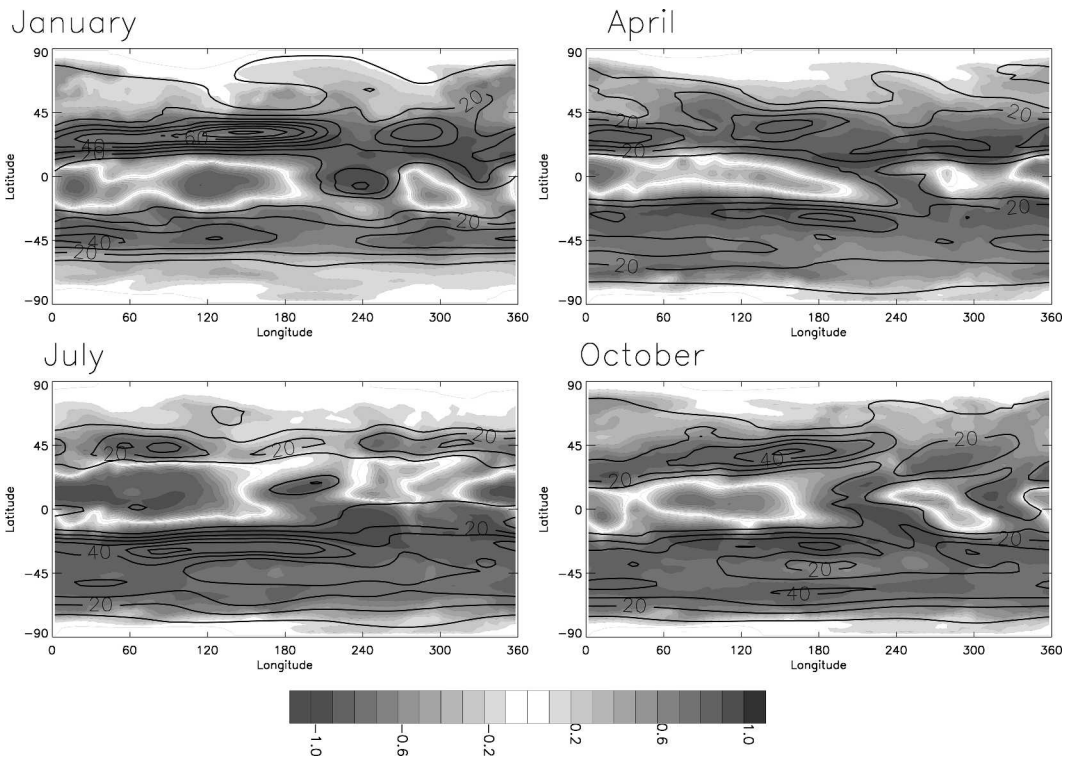

FIG. 9. Zonal anisotropy on the 101-hPa surface with contours of largest eastward wind below superimposed. The anisotropy is shown as gray shading with negative contours dashed; contour spacing is 0.1. Positive anisotropy means more eastward-propagating than westward-propagating pseudomomentum flux. The wind is shown as bold contours; contour spacing is 10 m s^{-1}. Average of 19 yr of GCM data.

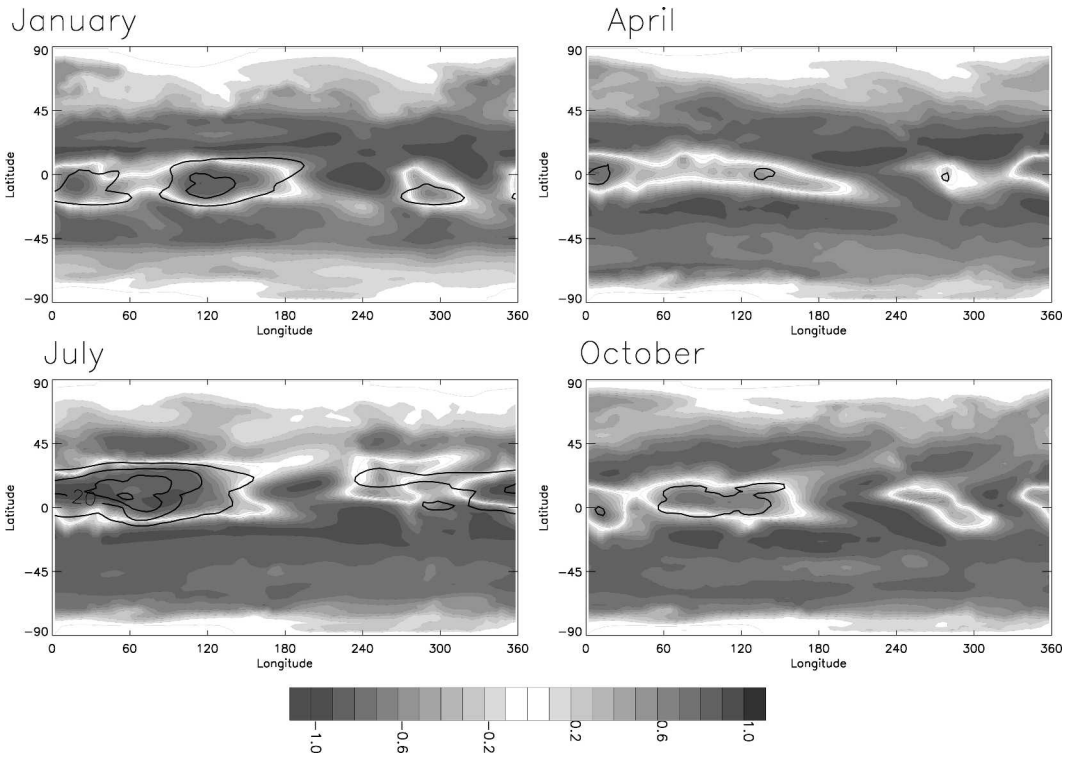

FIG. 10. As in Fig. 9 but with contours of largest westward wind below superimposed.

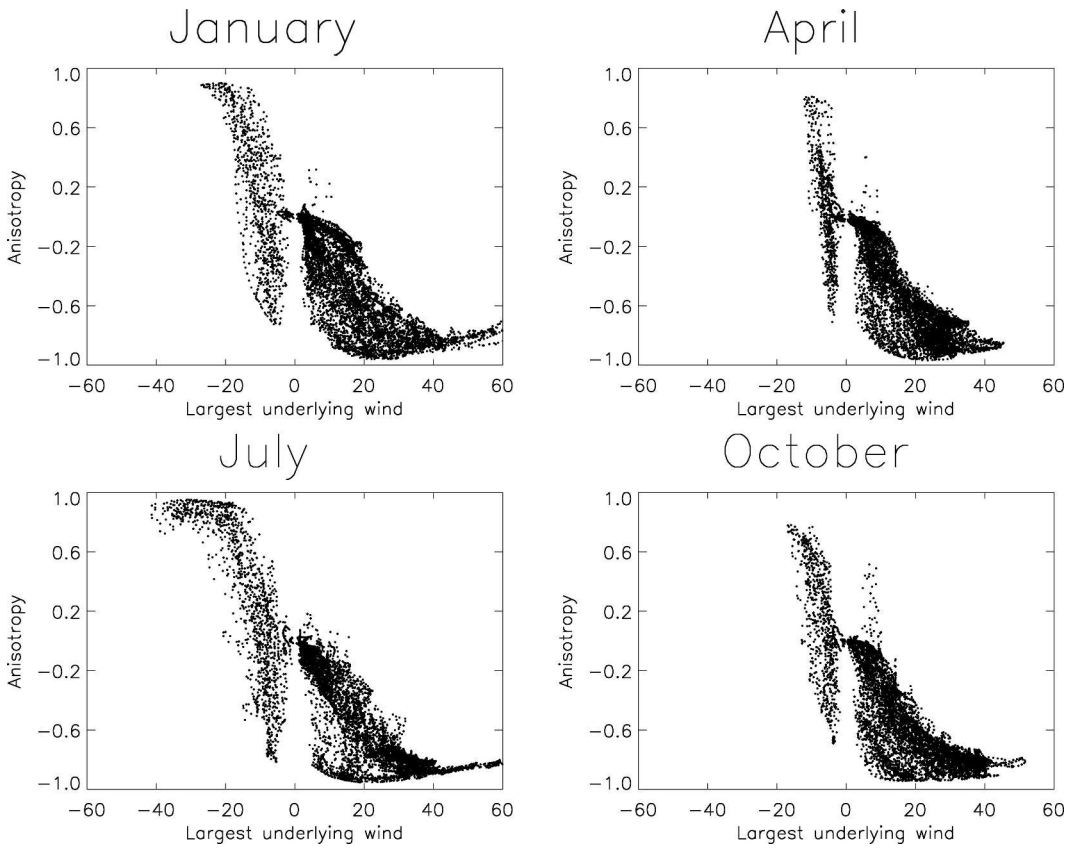

FIG. 11. Zonal anisotropy on a 101-hPa surface plotted as a function of largest magnitude underlying wind (a scatterplot of the data shown in Figs. 9 and 10). A positive underlying wind means that the largest magnitude underlying wind was eastward.

gravity wave spectrum at 101 hPa can largely be attributed to the changes in background wind below. Alexander (1998) reaches a similar conclusion: the changes in gross and net fluxes in the lower stratosphere can often be caused by the changes in the background wind.

The longitudinal structure in Figs. 9 and 10 shows remarkably little interannual variability (not shown). The one exception is northward of 45° for all months but especially for January in the northern winter when there are vortex-related wind and anisotropy patterns that differ significantly from year to year.

In the Tropics in January there are regions of large positive anisotropy extending from Africa to Indonesia (0°–180°E) and over South America (290°E) associated with underlying westward winds (Fig. 10). Negative anisotropy occurs over the east Pacific (240°E) and is associated with underlying eastward winds. In July the three main features are roughly in the same latitude and longitude range as in January. Again, in April there is a large positive anisotropy region from Africa to Indonesia; in October it is present but is divided into two positive anisotropy regions. The other large positive anisotropy region that was described above for January and July is also just visible in April and October. The large negative anisotropy region that was described above for January and July is still present but is a diffuse region separating the two positive anisotropy regions with no clear peak location in both the April and October plots. In all cases, the anisotropy pattern resembles the pattern in the underlying winds.

Figure 11 shows the relationship between zonal anisotropy and underlying wind. The zonal anisotropy generally becomes more negative as the largest underlying wind becomes more positive (Fig. 11) and vice versa. Further, the range of zonal anisotropy values decreases as the largest underlying wind increases in magnitude and the background wind dominates the filtering.

Figure 12 shows zonal anisotropy at 1 hPa. Superimposed are contours of maximum eastward wind between the launch level and 1 hPa, which is a measure of the filtering effect of the wind on the eastward propagating waves. It shows similar tropical and subtropical features to Fig. 9 from tropospheric filtering but the extratropics are strongly affected by stratospheric wind filtering and there is a complete reversal of zonal anisotropy between the lower and upper stratosphere in summer. Figure 13 shows zonal anisotropy at 1 hPa. As

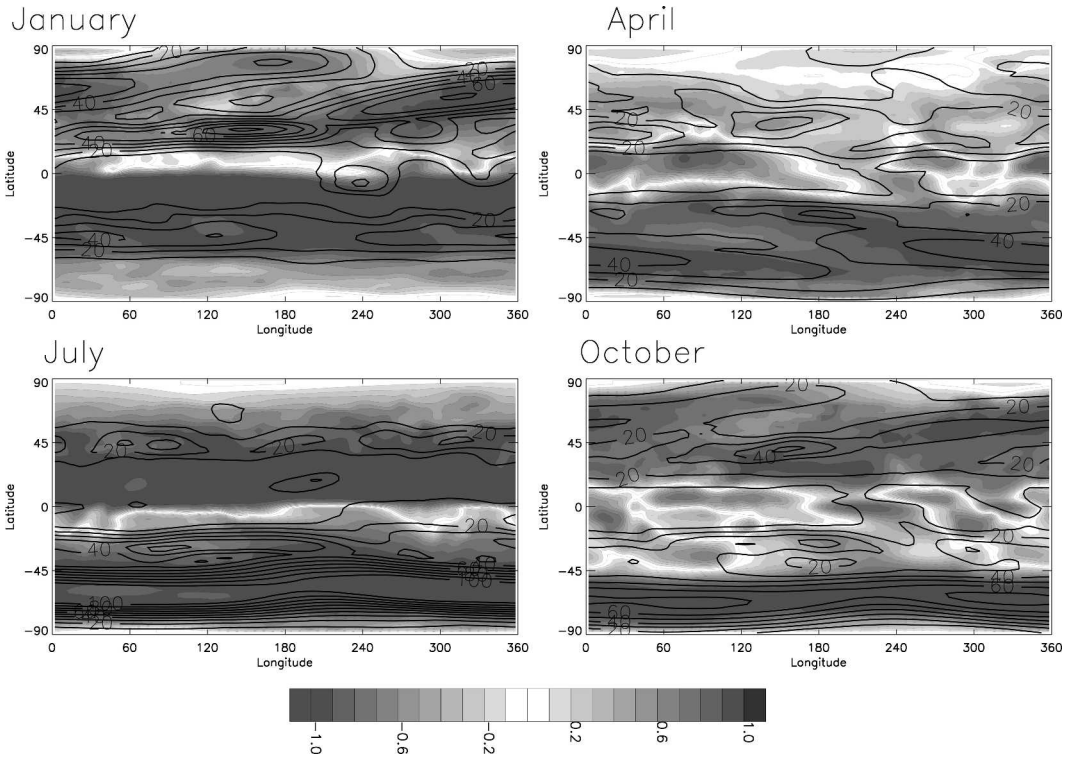

FIG. 12. Zonal anisotropy on the 1-hPa surface with contours of largest eastward wind below superimposed. The anisotropy is shown as gray shading with negative contours dashed; contour spacing is 0.1. Positive anisotropy means more eastward-propagating than westward-propagating pseudomomentum flux. The wind is shown as bold contours; contour spacing is 10 m s^{-1}. Average of 19 yr of GCM data.

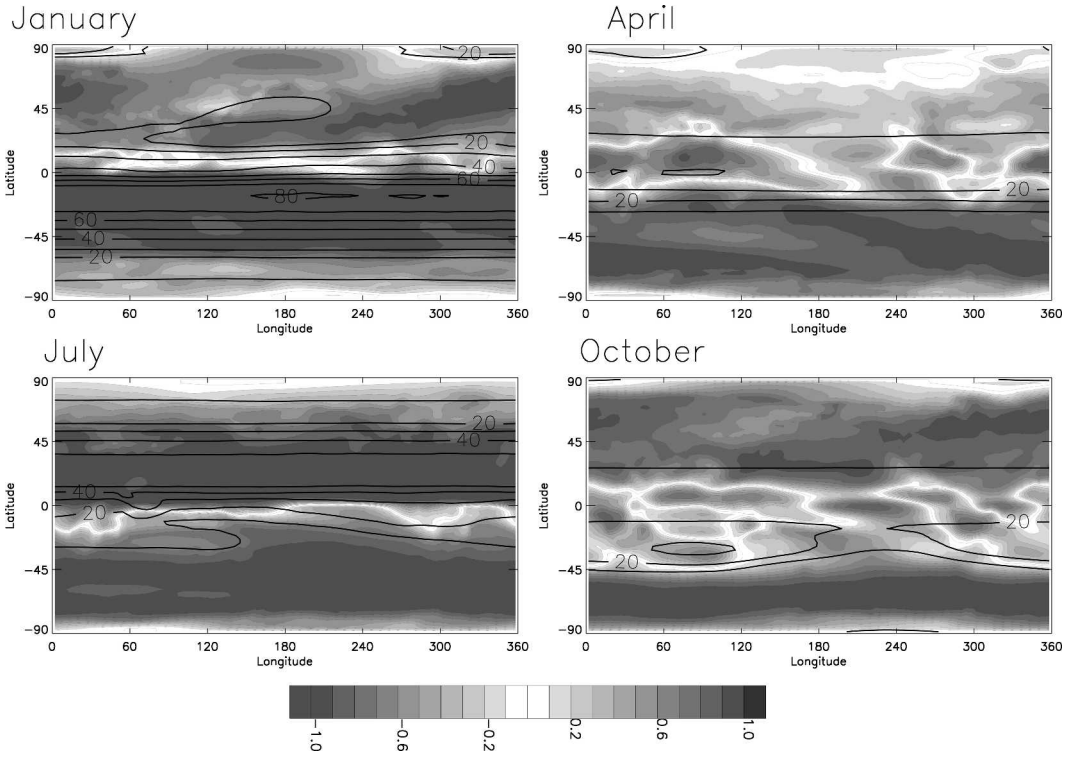

FIG. 13. As in Fig. 12 but with contours of largest westward wind below superimposed.

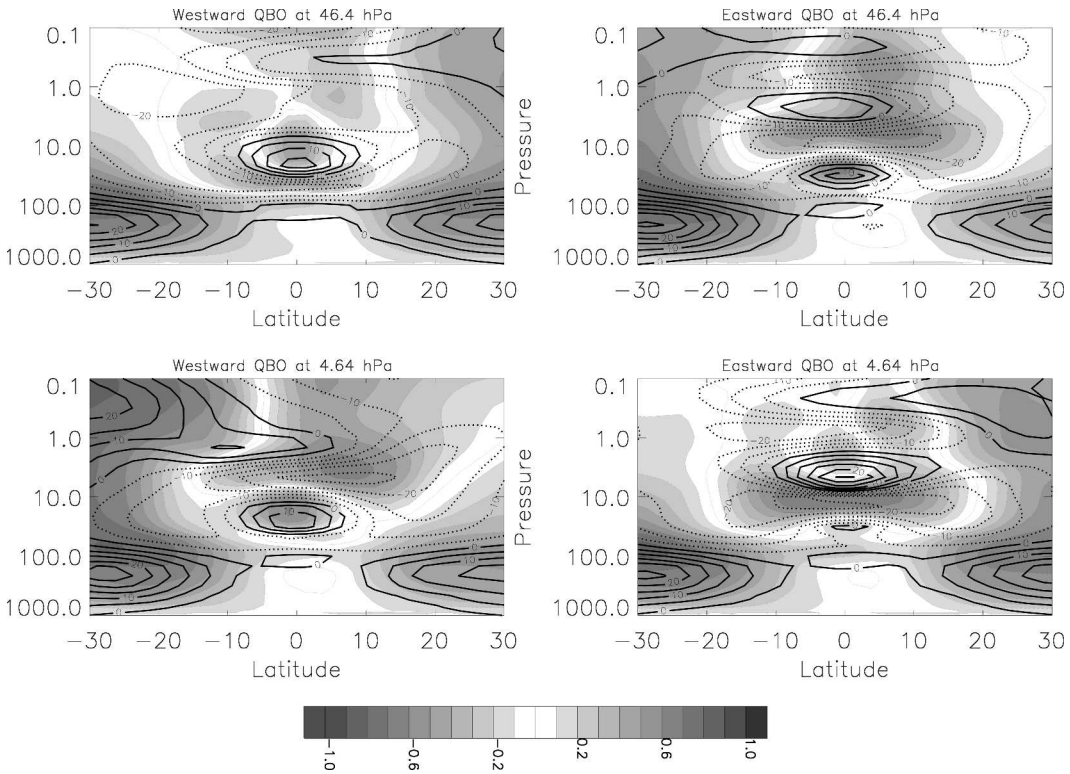

FIG. 14. Zonal mean zonal anisotropy with zonal mean zonal wind contours superimposed for QBO phases at 4.64 and 46.4 hPa. The anisotropy is shown as gray shading with negative contours dashed; contour spacing is 0.1. Positive anisotropy means more eastward-propagating than westward-propagating pseudomomentum flux. The zonal wind is shown as bold contours with negative contours dashed; contour spacing is 5 m s^{-1}. Pressure units for the vertical axis are hPa.

with Fig. 10, contours of the maximum westward wind between the ground and 1 hPa, which is a measure of the filtering effect of the wind on the westward-propagating waves, are superimposed.

The filtering effect of the stratosphere can be compared with the results of Dunkerton and Butchart (1984). They studied quasi-stationary waves and found that longitudinal structure during sudden warmings lead to selective transmission of gravity waves and so to a longitudinal variation in filtering. They found the average transmitted wavevector to be antiparallel to the average of the mean flow orientation in the underlying stratosphere. A similar effect can be seen in January in Fig. 12 where consistent longitudinal structure in underlying eastward wind, due to a displaced polar vortex, leads to a region of negative zonal anisotropy with peak values at 80°N, 180° and 55°N, 320°E. The region of large negative anisotropy is nearly coincident with the largest eastward wind below. Note that negative anisotropy implies that gravity waves propagating eastward have been selectively filtered out by the underlying atmosphere. The surviving waves are a mixture of those that propagating antiparallel to the zonal wind below (as in the Dunkerton and Butchart case) and those propagating parallel to the zonal wind below but with larger intrinsic phase speeds than the maximum zonal wind below. A similar longitudinal variation is seen in October in Fig. 12 but is less pronounced than in January. In July, the winds associated with the Antarctic polar vortex have much less average longitudinal variability. Correspondingly, there is little longitudinal structure in filtering effect and not much longitudinal variation in zonal anisotropy. A similar pattern of zonal anisotropy is seen in April in Fig. 12 but is less pronounced than in July.

6. Tropical filtering

Figure 14 shows zonal anisotropy with zonal wind contours composited for QBO phases at 46.4 and 4.64 hPa. Consider the composite of westward QBOs at 46.4 hPa in the top left panel of Fig. 14. At the equator, parameterized gravity waves propagate upward through small background winds below 100 hPa, which results in almost no change in anisotropy. From 100 to about 45 hPa the waves propagate through westward shear into westward background winds, which preferentially filters out westward-propagating waves, leading to a region of positive anisotropy (>0.3) centered just

above the maximum wind at about 35 hPa at 10°S–10°N. From 45 to about 12 hPa the waves propagate through eastward shear into eastward background winds, which preferentially filters out eastward-propagating waves leading to a region of negative anisotropy (<-0.2) centered just above the maximum wind at about 10 hPa at 4°S–4°N.

The patterns of anisotropy in the other three panels of Fig. 14 can be explained in a similar way. The location in altitude of the westward QBO phases has a more significant influence on anisotropy (because they span a larger latitude range) than the eastward QBO phases. For example, in the eastward QBO at 46.4-hPa case in the top right panel, at 8°N the background wind is westward over almost the entire altitude range and reaches a maximum near 10 hPa; this leads to strong positive anisotropy (>0.6) from 45 to 0.2 hPa.

Thus, it is also possible to account for the tropical distribution of zonal anisotropy by considering how the filtering effect of the background wind changes as the parameterized gravity waves propagate upward. The magnitude of the resulting gravity-wave-induced force at a given altitude is, however, more difficult to estimate from the background wind changes because it depends both on the net pseudomomentum flux per unit mass which survives filtering from winds well below the given altitude and on the filtering effect of winds near the given altitude. Thus, how much net flux is deposited depends on how the background wind varies with altitude in all of the atmosphere below.

We now turn to the effect that filtering has on the stratospheric semiannual oscillation (SAO). Ray et al. (1994) suggested that much of the interannual variability of the SAO strength can be accounted for by the QBO and that one reason for this is the filtering effect (or different transmissivity) of the lower stratosphere on vertically propagating waves including Kelvin waves and gravity waves. Thus, westward QBO winds do not filter Kelvin waves and eastward-propagating gravity waves do strongly filter westward-propagating gravity waves. The result is an enhanced eastward SAO phase (and presumably a diminished westward SAO phase) when the QBO is westward. Similarly, eastward QBO winds result in a diminished eastward SAO phase and an enhanced westward SAO phase. By taking appropriate composites for particular phases of the QBO and SAO, we test for these effects in our GCM.

Figure 15 shows zonal anisotropy with zonal wind contours composited for QBO phases at 4.64 hPa and for stratopause SAO phases. January and July are assumed to correspond to westward stratopause SAO phases, and April and October to eastward SAO phases. Figure 16 shows zonally averaged zonal gravity wave pseudomomentum flux and zonal wind profiles at 1.25°S (closest GCM latitude to the equator).

The top left-hand panels of Figs. 15 and 16 show the westward QBO, westward SAO case. In this case we expect westward-propagating gravity waves to be strongly filtered by the QBO. The top left-hand panel of Fig. 16 shows this behavior; the eastward-propagating gravity wave flux is little changed over the range 15–4.9 hPa while the westward-propagating flux decreases by more than an order of magnitude. The local maximum in wind near 1.7 hPa halts further breaking of westward-propagating waves but is not strong enough to cause significant breaking of eastward-propagating waves. Figure 15 shows the anisotropy increasing (i.e., becoming less negative) through the westward QBO winds and reaching 0 at 6.1 hPa, so filtering is as Ray et al. (1994) suggests. However, although the QBO westward phase undoubtedly increases the anisotropy of the gravity wave spectrum, the result is a spectrum that is essentially isotropic rather than one with positive anisotropy.

The top right-hand panels of Figs. 15 and 16 show the eastward QBO, westward SAO case. In this case we expect westward-propagating gravity waves to be largely unfiltered by the eastward QBO phase and for eastward-propagating gravity waves to be strongly filtered. Figure 16 shows this behavior; westward-propagating flux is little changed over the range 15–3 hPa while the eastward-propagating flux decreases by more than an order of magnitude. Figure 15 shows the anisotropy decreasing through the eastward QBO winds and reaching a minimum value near zero at 6.8 hPa, so once again filtering is as Ray et al. (1994) suggests. Further, comparing the top left and right panels of Fig. 16, the westward SAO is strongest when the underlying QBO is eastward.

The lower left-hand panels of Figs. 15 and 16 show the westward QBO, eastward SAO case. We again expect westward-propagating gravity waves to be strongly filtered as is seen to be the case in Fig. 16. This strong filtering is also seen in Fig. 15 where anisotropy increases as waves propagate through the westward QBO phase reaching a maximum positive anisotropy at 3.2 hPa. The eastward SAO phase is clearly visible in the two figures. The lower right-hand panels of Figs. 15 and 16 show the eastward QBO, eastward SAO case. In this case we expect eastward-propagating gravity waves to be strongly filtered, which is indeed seen to be the case in Fig. 16. The anisotropy decreases (see Fig. 15) as waves propagate through the eastward QBO phase but remains positive up to the stratopause. There is no evidence of an eastward phase of the stratospheric SAO in this month. Gravity wave filtering is, once again, as Ray et al. (1994) suggests. Further, the eastward SAO/eastward QBO case (lower right panel) is diminished (to the point where winds are no longer eastward) relative to the westward QBO case (lower left panel).

7. Conclusions

We compared GCM parameterized and observational azimuthal distributions of gravity wave fluxes at

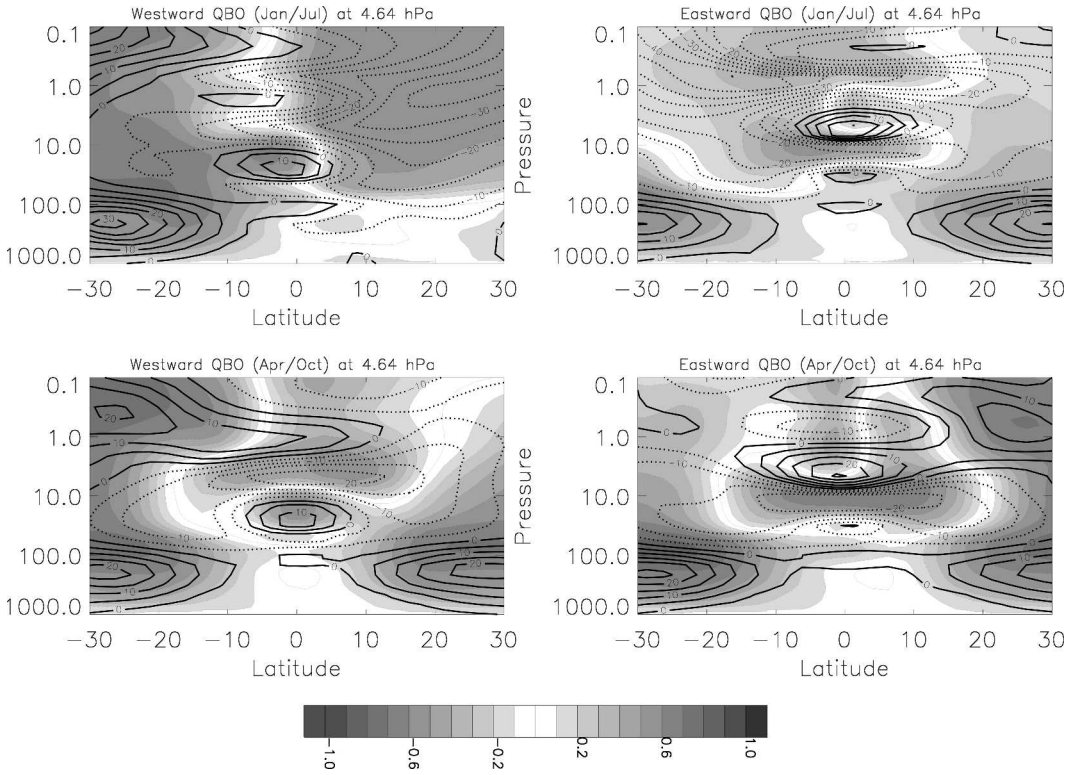

FIG. 15. Zonal mean zonal anisotropy with zonal mean zonal wind contours superimposed for QBO phases at 4.64 hPa. (top left) Composite of westward phase of the QBO, westward phase of the SAO (i.e., Jan and Jul); (top right) composite of eastward phase of the QBO, westward phase of the SAO; (bottom left) composite of westward phase of the QBO, eastward phase of the SAO (i.e., Apr and Oct); (bottom right) composite of eastward phase of the QBO, eastward phase of the SAO. The anisotropy is shown as gray shading with negative contours dashed; contour spacing is 0.1. Positive anisotropy means more eastward-propagating than westward-propagating pseudomomentum flux. The zonal wind is shown as bold contours with negative contours dashed; contour spacing is 5 m s^{-1}. Pressure units for the vertical axis are hPa.

tropical and midlatitude sites. The agreement between the GCM parameterized and observational azimuthal distributions at Nancy (48°N) is good. This suggests that, at midlatitudes, observed gravity wave fluxes in the stratosphere may largely be determined by filtering and that the assumption that gravity wave sources are isotropic and near the ground could be good enough for current GCMs. The agreement between the GCM parameterized and observational results in the Tropics at Atuona is much less good; indeed, the results differ even when the averaged background wind looks broadly similar. However, launching parameterized waves from a higher altitude leads to better agreement. This suggests that, in the Tropics, a higher source altitude, possibly because of the height of convective activity, may be more appropriate.

We examined zonal anisotropy and net parameterized pseudomomentum flux to investigate the gravity wave filtering that results from changes in the background wind and background density with altitude. We found that big changes in zonal mean zonal anisotropy occur as gravity wave spectra propagate through the tropospheric subtropical jets leading to the shadows of large negative zonal anisotropy that are clearly seen in the lower stratosphere in summer. The corresponding net zonal mean pseudomomentum fluxes are, of course, of the same sign as the zonal anisotropy, but the plots are complicated by the effect of the background density; on the one hand, regions of similar anisotropy can have fluxes that differ by several orders of magnitude and, on the other hand, regions of similar zonal pseudomomentum flux can have zonal anisotropies that differ greatly.

Wave-induced forces per unit mass (accelerations) were largest where large amounts of net flux per unit mass are being deposited. Thus the conditions that promote large wave-induced forces per unit mass are as stated in section 4: first, an atmosphere well below that has preferentially filtered out waves propagating in one direction over another leading to a large net pseudomomentum flux; second, a sufficiently high altitude for a low background density and thus a large net pseudomomentum flux per unit mass; and third, background wind shear that is filtering out waves propagating in the direction of the net pseudomomentum flux.

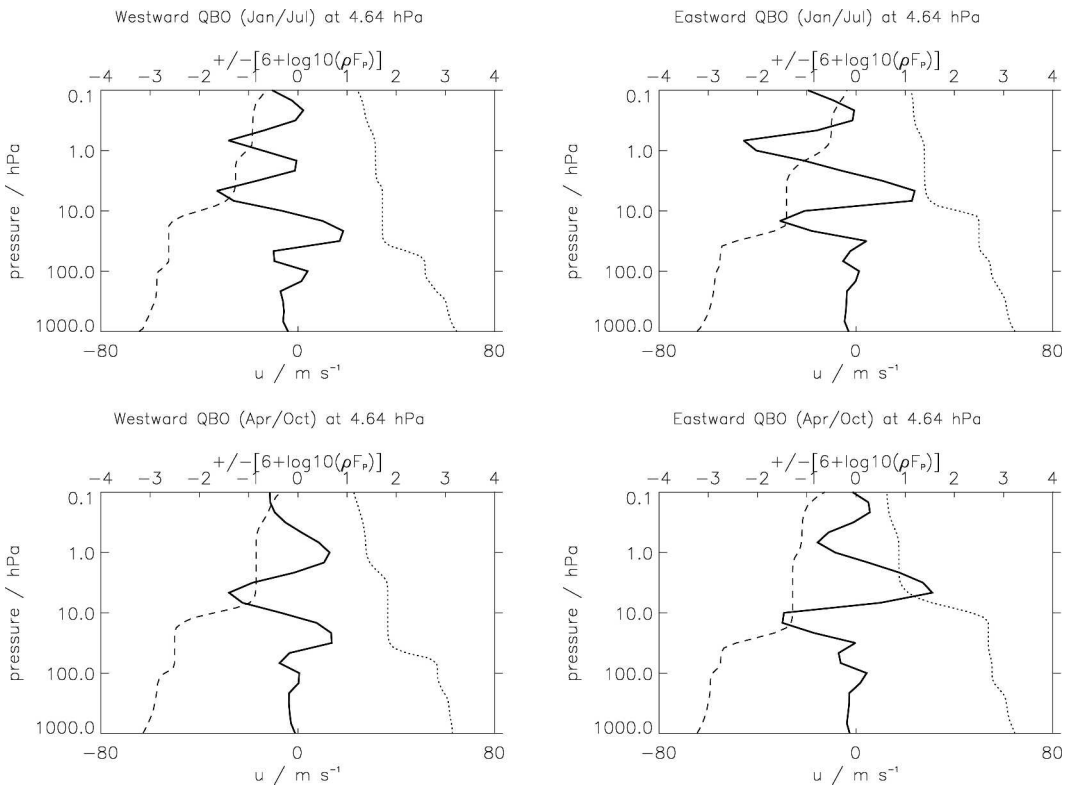

FIG. 16. Zonal gravity wave pseudomomentum flux and zonal wind profiles zonally averaged at 1.25°S (nearest GCM latitude to the equator). The panels are arranged as in Fig. 15. The upper x scale is for the fluxes and is logarithmic, units are $\log_{10}(\text{kg m}^{-1}\text{ s}^{-2})$. On the positive x axis, $+[6 + \log_{10}(\rho \mathbf{F}_p)]$ is plotted for eastward-propagating fluxes (dotted curve). On the negative x axis, $-[6 + \log_{10}(\rho \mathbf{F}_p)]$ is plotted for westward-propagating fluxes (dashed curve). The lower x scale is for the zonal wind (bold solid curve), units are m s^{-1}.

We showed the zonal anisotropy as a function of latitude and longitude near the tropopause and stratopause. At the tropopause the shadowing effect of the jets, evident in the zonal average, also has some longitudinal structure. To good approximation, the areas of large negative zonal anisotropy coincide with the areas of largest eastward wind below and the areas of large positive anisotropy with largest westward wind below. This suggests that much of the anisotropy at the tropopause can be attributed to changes in the background wind below—a conclusion supported by Alexander (1998). Near the stratopause the correspondence of zonal anisotropy with winds below is less good, particularly in the Tropics. This is to be expected given that the history of the parameterized gravity spectrum is often more complicated, as the spectrum may pass through several altitude ranges of different wind shear, particularly in the Tropics.

We looked more closely at tropical filtering. We examined composite averages at particular phases of the QBO and found that, almost invariably, the anisotropy increases just below the QBO wind extrema and the resulting peak anisotropy occurs just above the QBO wind extrema. The filtering effect of the QBO was seen to depend on its phase, with gravity waves propagating in the same direction as the QBO phase being strongly filtered and gravity waves propagating in the opposite direction to the QBO phase being weakly filtered. The strength of our GCM stratospheric SAO was seen to depend on the phase of the QBO beneath in the manner suggested by Ray et al. (1994). Thus the SAO is seen to be stronger when the QBO in the midstratosphere is in the opposite phase, for example, eastward SAO above westward QBO.

Finally it should be noted that the gravity wave parameterization that we have used in these studies is applied independently in each vertical column and the effects are transferred horizontally indirectly through changes in the resolved winds and temperature. Applying the parameterization independently to each vertical column is only a good approximation if the horizontal propagation of parameterized gravity waves is small compared to the distance between the grid points of the GCM. In reality, under conditions where the vertical group velocity becomes small relative to the horizontal group velocity, gravity waves can propagate horizontally over very large distances (e.g., Sato 2000), but such horizontal propagation is a subject for future study if and when fully three-dimensional gravity wave parameterizations have been developed.

Acknowledgments. This work was supported by the research programme of the U.K. Met Office. C. D. Warner received support from the Natural Environment Research Council through Grant NER/A/S/2000/00452. We thank C. Souprayen at the Service d'Aeronomie for the radiosonde data used to compile the azimuthal sector plots in Figs. 1 and 2. We thank three anonymous reviewers for their suggestions, which have led to important improvements to this paper.

REFERENCES

Alexander, M. J., 1998: Interpretations of observed climatological patterns in stratospheric gravity wave variance. *J. Geophys. Res.,* **103,** 8627–8640.

——, and T. J. Dunkerton, 1999: A spectral parameterization of mean-flow forcing due to breaking gravity waves. *J. Atmos. Sci.,* **56,** 4167–4182.

——, and R. A. Vincent, 2000: Gravity waves in the tropical lower stratosphere: A model study of seasonal and interannual variability. *J. Geophys. Res.,* **105,** 17 983–17 993.

Beres, J. H., M. J. Alexander, and J. R. Holton, 2002: Effects of tropospheric wind shear on the spectrum of convectively generated gravity waves. *J. Atmos. Sci.,* **59,** 1805–1824.

Butchart, N., J. Austin, J. R. Knight, A. A. Scaife, and M. L. Gallani, 2000: The response of the stratospheric climate to projected changes in well-mixed greenhouse gases from 1992 to 2051. *J. Climate,* **13,** 2142–2159.

Charron, M., and E. Manzini, 2002: Gravity waves from fronts: Parameterization and middle atmosphere response in a general circulation model. *J. Atmos. Sci.,* **59,** 923–941.

Cullen, M. J. P., 1993: The unified forecast/climate model. *Meteor. Mag.,* **122,** 81–94.

Dunkerton, T. J., and N. Butchart, 1984: Propagation and selective transmission of internal gravity waves in a sudden warming. *J. Atmos. Sci.,* **41,** 1443–1460.

Fritts, D. C., and W. Lu, 1993: Spectral estimates of gravity wave energy and momentum fluxes II: Parameterization of wave forcing and variability. *J. Atmos. Sci.,* **50,** 3695–3713.

——, and T. E. VanZandt, 1993: Spectral estimates of gravity wave energy and momentum fluxes I: Energy dissipation, acceleration and constraints. *J. Atmos. Sci.,* **50,** 3685–3694.

Gregory, D., and P. R. Rowntree, 1990: A mass flux convection scheme with representation of cloud ensemble characteristics and stability-dependent closure. *Mon. Wea. Rev.,* **118,** 1483–1506.

——, G. J. Shutts, and J. R. Mitchell, 1998: A new gravity-wave-drag scheme incorporating anisotropic orography and low-level wave breaking: Impact upon the climate of the UK Meteorological Office Unified Model. *Quart. J. Roy. Meteor. Soc.,* **124,** 463–493.

Hines, C. O., 1997: Doppler spread parameterization of gravity wave momentum deposition in the middle atmosphere. Part 1: Basic formulation. *J. Atmos. Terr. Phys.,* **59,** 371–386.

Holton, J. R., 1982: The role of gravity wave-induced drag and diffusion in the momentum budget of the mesosphere. *J. Atmos. Sci.,* **39,** 791–799.

Lawrence, B. N., 1997: Some aspects of the sensitivity of stratospheric climate simulation to model lid height. *J. Geophys. Res.,* **102,** 23 805–23 811.

Lindzen, R. S., 1981: Turbulence and stress due to gravity wave and tidal breakdown. *J. Geophys. Res.,* **86,** 9707–9714.

McFarlane, N. A., 1987: The effect of orographically excited gravity wave drag on the general circulation of the lower stratosphere and troposphere. *J. Atmos. Sci.,* **44,** 1775–1800.

Medvedev, A. S., and G. P. Klaassen, 1999: Parameterization of gravity wave momentum deposition based on nonlinear wave interactions: Basic formulation and sensitivity tests. *J. Atmos. Terr. Sol. Phys.,* **62,** 1015–1033.

Palmer, T. N., G. J. Shutts, and R. Swinbank, 1986: Alleviation of a systematic westerly bias in general circulation and numerical weather prediction models through an orographic wave drag parameterisation. *Quart. J. Roy. Meteor. Soc.,* **112,** 1001–1039.

Ray, E. A., J. R. Holton, E. F. Fishbein, L. Froidevaux, and J. W. Waters, 1994: The tropical semiannual oscillations in temperature and ozone as observed by the MLS. *J. Atmos. Sci.,* **51,** 3045–3052.

Ricciardulli, L., and R. Garcia, 2000: The excitation of equatorial waves by deep convection in the NCAR Community Climate Model (CCM3). *J. Atmos. Sci.,* **57,** 3461–3484.

Sato, K., 2000: Sources of gravity waves in the polar middle atmosphere. *Adv. Polar Upper Atmos. Res.,* **14,** 233–240.

——, and T. J. Dunkerton, 1997: Estimates of momentum flux associated with equatorial Kelvin and gravity waves. *J. Geophys. Res.,* **102,** 26 247–26 261.

Scaife, A. A., N. Buchart, C. D. Warner, D. Stainforth, W. Norton, and J. Austin, 2000: Realistic quasi-biennial oscillations in a simulation of the global climate. *Geophys. Res. Lett.,* **27,** 3481–3484.

——, ——, ——, and R. Swinbank, 2002: Impact of a spectral gravity parameterization on the stratosphere in the Met Office Unified Model. *J. Atmos. Sci.,* **59,** 1473–1489.

Warner, C. D., and M. E. McIntyre, 1996: On the propagation and dissipation of gravity wave spectra through a realistic middle atmosphere. *J. Atmos. Sci.,* **53,** 3213–3235.

——, and ——, 1999: Toward an ultra-simple spectral gravity wave parameterization for general circulation models. *Earth Planets Space,* Vol. 51, Terra Scientific, 475–484.

——, and ——, 2001: An ultrasimple spectral gravity wave parameterization for nonorographic gravity waves. *J. Atmos. Sci.,* **58,** 1837–1857.